Applied Surface Science 639 (2023) 158235

Contents lists available at ScienceDirect

Applied Surface Science

journal homepage: www.elsevier.com/locate/apsusc

Full Length Article

A multi-timescale model predicts the spherical-to-cubic morphology crossover of magnetron-sputtered niobium nanoparticles

Pavel Pleskunov [a,*], Tereza Košutová [b], Mariia Protsak [a], Marco Tosca [a,c], Kateryna Biliak [a], Daniil Nikitin [a], Zdeněk Krtouš [a], Jan Hanuš [a], Jiří Houška [d], Miroslav Cieslar [e], Suren Ali-Ogly [a], Peter Kuš [f], Ondřej Kylián [a], Andrei Choukourov [a,*]

[a] Department of Macromolecular Physics, Faculty of Mathematics and Physics, Charles University, V Holešovičkách 2, 180 00 Prague, Czech Republic
[b] Department of Condensed Matter Physics, Faculty of Mathematics and Physics, Charles University, Ke Karlovu 5, 121 16 Prague, Czech Republic
[c] Extreme Light Infrastructure (ELI)-Beamlines Center, Institute of Physics (FZU), Czech Academy of Sciences, Dolní Břežany, 252 41, Czech Republic
[d] Department of Physics and NTIS–European Centre of Excellence, University of West Bohemia, Univerzitní 8, 301 00 Plzeň, Czech Republic
[e] Department of Physics of Materials, Faculty of Mathematics and Physics, Charles University, Ke Karlovu 5, Prague 121 16, Czech Republic
[f] Department of Surface and Plasma Science, Faculty of Mathematics and Physics, Charles University, V Holešovičkách 2, Prague 180 00, Czech Republic

ARTICLE INFO

Keywords:
Nanocluster temperature
Molecular dynamics
Sputtering
Nanoparticles
Multiscale simulations

ABSTRACT

Sputter-based cluster beam deposition offers a solvent- and effluent-free physical method to synthesize nanoparticles (NPs) with tailored characteristics. Despite the broad capabilities to control the NP architecture via multiple parameters such as magnetron power, gas pressure and flow, type of gas, etc., the technique is still far from being at hand because of insufficient understanding of the processes of NP nucleation, growth, and transport. Here, we synthesize Nb NPs of spherical (diameter 32 nm) and cubic (side length 19 nm) shape, depending on pressure, and perform a detailed structural characterization. A known analytical model of the NP growth and thermalization was modified to account for ion bombardment and non-ideal atomic sticking in the plasma. The model was enforced with ad hoc multi-timescale molecular dynamic simulations to unveil the peculiarities of the growth of Nb NPs and explain the difference in their morphology.

1. Introduction

For past decades, plasma-assisted vacuum-based techniques have emerged as a powerful toolset for the manufacturing of a wide range of materials. From the plethora of techniques, magnetron sputtering has attained significant interest and has been quickly adopted [1]. Nowadays, magnetron sputtering is considered a versatile thin film deposition method that has relatively low operational costs and is compatible with an existing stack of "dry" processes. Besides thin films, technological advancements have created a demand for different kinds of nanostructured materials, giving rise to the development of cluster beam deposition [2].

In the early 1990 s, the Freiburg group employed magnetron sputtering for metal vaporization in a gas aggregation cluster source (GAS) [3,4]. A core principle at the heart of the technique is the sputtering of metal with energetic buffer gas ions (for example, Ar or Xe) [5] with the formation of super-saturated atomic metal vapors that subsequently condensate to form clusters or nanoparticles (NPs). Newly created NPs are then transferred by the gas flow from the plasma region through the volume of the aggregation chamber, towards the exiting orifice. The NPs grow via the deposition of metal atoms on their way to the substrate. Although this approach offers a number of advantages, such as flexibility and control over NP size and composition [6–8], magnetron-based GAS systems have received limited popularity, mainly in academia. The lack of understanding of the underlying physical processes is what hindered the rate of adoption of GAS systems by industry.

One crucial issue restricting the wide adoption of magnetron-based GASes is the precise control over cluster morphology and, more importantly, its predictability. A common approach relies on the assumption that in most cases, the final shape of NPs is governed by surface energy minimization. Therefore, close-to-spherical NPs with the lowest surface-to-volume ratio are formed during the aggregation process. On the other hand, engineering of the desired NP morphology (which is rarely spherical) at the nanometer scale is beneficial for

* Corresponding authors.
E-mail addresses: pleskunov@kmf.troja.mff.cuni.cz (P. Pleskunov), choukourov@kmf.troja.mff.cuni.cz (A. Choukourov).

https://doi.org/10.1016/j.apsusc.2023.158235
Received 7 June 2023; Received in revised form 23 July 2023; Accepted 10 August 2023
Available online 11 August 2023
0169-4332/© 2023 Elsevier B.V. All rights reserved.

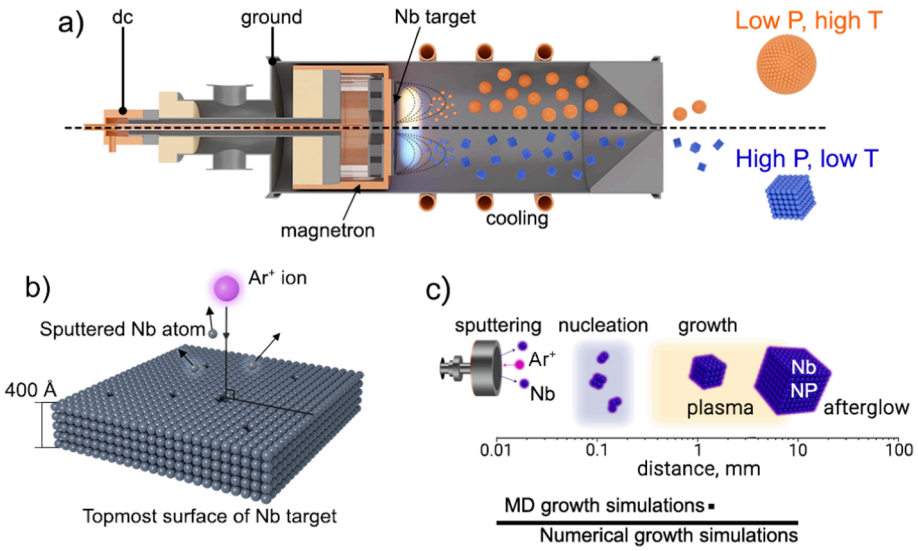

Fig. 1. The scheme of (a) gas aggregation cluster source (GAS) used for the production of Nb NPs (the difference in operational conditions is denoted by color, 13 Pa correspond to the low pressure and 75 Pa to high pressure), (b) SRIM/TRIM simulation model and (c) spatial ranges for molecular dynamic and numerical simulations as they relate to aggregation chamber length.

numerous applications, ranging from catalysis [9–11] and fuel cells [12] to photonics [13–16] and biomolecule detection [17]. The formation of other-than-spherical NP morphologies with larger surface-to-volume ratios is difficult to predict with the surface energy minimization processes alone.

Numerous attempts have been made to create a roadmap for predicting the NP morphology or, at the very least, mapping them to a specific set of experimental parameters when using "wet" chemistry [18–23]. Magnetron-sputtering inert gas condensation provides multiple degrees of freedom in terms of NP morphology control. In general, this problem could be approached by either introducing mass filtration mechanisms or tailoring the operational parameters. A good example of gaining control over the NP morphology via mass selection was demonstrated by Nielsen *et al* [24]. However, it should be noted that mass filtering of any kind is always associated with material losses and longer deposition times.

On the other hand, tailoring experimental conditions may become a great trade-off between the selectivity of the process and material utilization/processing time. For instance, magnetron power has been reported to have a profound effect on atomic flux and the NP temperature during its growth. In combination with surface diffusion rates governed by energetic barriers arising from the crystal structure, this allows for the synthesis of Fe NP of cubic morphology [25]. When using radio-frequency powered plasma, the NP shape can be manipulated by adjusting the duty cycle, as has been reported for W NPs [26].

The fact that NP nucleation and growth occurs in the vicinity of the sputtering target opens a possibility to manipulate the magnitude of the magnetic field (and, therefore, plasma confinement that affects the temperature and density of sputtered atoms) by linearly displacing the magnetic circuit with respect to the target [27] or by varying thickness of the targets of high magnetic permeability, which in turn results in magnetic screening effect [28]. An alternative pathway to the NP shape tuning involves finding a combination of materials with different nucleation/growth kinetics. For example, Vernieres *et al.* demonstrated a concept of selective wetting of specific surface sites on pre-condensed Fe NPs by gold atoms resulting in multiple-frame Fe-Au cubic morphology [29].

In recent years, the importance of buffer gas composition/pressure (flow rate) in the formation of NPs has been reconsidered and extensively scrutinized. Wang *et al.* demonstrated an influence of the Ar/He ratio on the deposition rate and the resulting NP morphology [30]. The Kiel group has demonstrated a concept of controlling the NP composition by adjusting operational pressure in the aggregation chamber that resulted in an alternation of the erosion track width [31,32]. Later, Drewes *et al.* showed that working pressure and gas flow are responsible for spatial shifts of the NP trapping region [33,34]. This approach takes advantage of NP electrostatic trapping phenomena [35] with the aim to control the residence time of the NPs in the "hot" plasma zone and therefore influence its temperature. Finally, computational fluid dynamics (CFD) simulations became an insightful complement to the experimental investigation, showing a strong influence of the geometry of the aggregation chamber and the working pressure on NP transport inside the aggregation chamber [36,37]. Despite many extensive studies, there exists a vast gap between atomistic simulations focusing on the NP nucleation and growth and CFD simulations that consider mostly transport phenomena inside the cluster systems. Recently, an attempt has been made to bridge this gap using large-scale molecular dynamics (MD) simulations to track down the NP as it flows throughout the aggregation chamber [38]. Moreover, a multiscale MD framework was developed to enable consistent modelling of sputtering, transport and deposition processes. The framework interconnected the MD model and experiments allowing to extract time-dependent macroscopic parameters (for example, reaction and/or deposition rates), often unattainable otherwise. A great potential of the suggested methodology was demonstrated by modelling the growth of the platinum NPs on the carbon electrode in a proton-exchange membrane fuel cell [39,40].

In the current work, we aim to contribute to a rapidly evolving field of magnetron-sputtering inert gas condensation by performing a detailed structural characterization followed by *ad hoc* multi-timescale simulations to unveil the peculiarities of the niobium nanoparticles (Nb NPs) growth. In our previous work, we employed a cluster system to prepare Nb NPs of cubic morphology, which has become an onset for this study [17]. It focuses on the phenomena governing the NP morphology to provide a roadmap for future research on gas-phase NP synthesis. The effects of the temperature regime, atomic "precursor" and sticking coefficients on the NP shape are investigated. We also demonstrate a way of independently tuning the NP shape concerning its crystal structure or composition by simply readjusting the gas pressure.

2. Material and methods

2.1. Sample preparation

Nb NPs were synthesized using a magnetron-sputtering inert gas condensation system (schematically depicted in Fig. 1**a**) as described in detail in previous papers and summarized here very briefly [17,41]. A 3-inch Nb target (Kurt J. Lesker Ltd, 99.99 % purity, 0.125-inch thick) was used. The system was evacuated to a base pressure of 10^{-5} Pa, then a buffer gas-carrier (Ar, 99.996 % purity, Linde Gas) was introduced into the GAS. The Ar flow was adjusted to 2 sccm and 20 sccm to create pressures of 13 Pa and 75 Pa, respectively. The pressure was probed by a capacitance gauge (626C, MKS Baratron®, full range is 1 Torr, typical accuracy 0.25% of the full range) connected to the aggregation chamber via a transversal port located at the middle of the chamber's full length. To ensure the pressure readings are relevant for the entire volume of the aggregation chamber, the computational fluid dynamics (CFD) simulations are performed (see Section 2.7 for the details). When operated at the selected flow rates (2 and 20 sccm for 13 Pa and 75 Pa, respectively), our system exhibits small longitudinal pressure gradient across entire aggregation chamber that is, perhaps, even out-of-the instrument sensitivity (**Figure S1**). A dc power supply (Kurt J. Lesker Ltd, TruPlasma DC 3001) was operated in a constant current mode with the current set to 500 mA. The retractable quartz crystal microbalance (QCM) was inserted into the deposition chamber normally to the NP beam via a load-lock and aligned below the GAS exit nozzle at a distance of 150 mm to match the sample position. It was retracted after the deposition rate stabilized. Substrates were introduced into the deposition chamber in a similar manner.

2.2. Sample characterization

Two types of substrates were used to collect Nb NPs: carbon-coated copper grids (SPI Supplies, Structure Probe, Inc.) for High-Resolution Transmission Electron Microscopy (HRTEM) and silicon wafers (OnSemi, ⟨100⟩, one-side polished, 525 μm thick) to perform Scanning Electron Microscopy (SEM), Small Angle X-ray Scattering (SAXS), and X-ray diffraction (XRD). The Si wafers were cleaned by ultrasonication in acetone and ethanol prior to use.

An in-depth analysis of the NP morphology was carried out using a Transmission Electron Microscope (TEM, 2200FS, Jeol Ltd, Japan) equipped with a FEG cathode operated at 200 kV of acceleration voltage and a Centurio Large Angle SDD-EDX detector. In addition, a T-FE-based Scanning Electron Microscope (SEM, JSM-7200F, Jeol Ltd., Tokyo, Japan) was employed for a complementary analysis of the Nb NP shape and size distribution. All SEM measurements were carried out in a top-view orientation at the 25-kV acceleration voltage.

Small-angle X-ray scattering (SAXS) analysis became a primary tool for probing the NP size distribution, as it provides extensive statistics. The SAXS measurements were performed in transmission geometry using a Xenocs Xeuss 2.0 SAXS instrument (Mo X-ray source ($\lambda_{Mo\ K\alpha}$ = 0.07107 nm), a hybrid pixel array detector Dectris Pilatus 200 k). All SAXS measurements were conducted at a fixed sample-to-detector distance of 2500 mm. After azimuthal integration, background correction and normalization, the resulting 1D SAXS curves were fitted to obtain the volume distribution of the NPs using the Irena data manipulation and analysis toolbox[42] available for the IGORpro package. For the NP structural analysis, Powder X-ray Diffraction (XRD) analysis was performed using a diffractometer (XRD, Rigaku SmartLab) rigged with a rotating X-ray source ($\lambda_{Cu\ K\alpha}$ = 0.15418 nm) in a parallel beam geometry. The angle of incidence of the primary beam of $\omega = 0.6^{\circ}$ was maintained for all measurements. The diffraction pattern fitting was performed using the MStruct package [43].

2.3. SRIM/TRIM calculations of Nb sputtering yield

The Stopping and Range of Ions in Matter (SRIM) simulations have been performed to analyze the total sputtering yield of the Nb target, depending on the experimental conditions. The SRIM models the collision cascade produced when a high-energy ion collides with a solid target. In general, the SRIM code relies on the binary collision approximation. Thus, the collisions between atoms are approximated by successive elastic binary collisions described by a binary interaction potential and energy losses.

In this work, the SRIM-2013 software package is used [44]. We opt for a detailed calculation with full damage cascades to trace every recoiling atom until its energy drops below the lowest displacement energy of any target atom. It is assumed that singly charged Ar ions approach the target surface with energy equivalent to the dc bias of 145 – 190 V.

The number of inbound Ar ions is set to 10^5 to harvest statistically meaningful data for the evaluation of the sputtering yields. The cascades which come back to the target surface are important in our case and are of our primary interest. Therefore, we simulate a thin target (40 nm) which provides an adequate approximation for processes that involve relatively heavy ions (e.g. >20 amu, whereas Ar^+ has a mass of 39.9 amu). We focus mainly on the estimation of the sputtering yield of ion projectiles incoming at a normal angle towards the target surface (Fig. 1**b**).

The displacement energy (i.e. minimum energy required to knock a target atom off the lattice site to a distance that does not allow for immediate re-deposition) of 25 eV is used, which is typical for most of the metals. The lattice binding energy typically lies in the range of 1–3 eV, so we kept the pre-defined value of 3 eV as supplied with the SRIM software database. The surface binding energy (SBE) affects the sputtering yield the most, while both the displacement energy and the lattice binding energy have only a minor effect. By default, the SRIM code approximates the surface binding energy with the heat of sublimation per atom. However, these two quantities are not necessarily the same since the energy threshold for the atoms leaving the surface also depends on the surface morphology, composition, and other factors.

When used with default SBE values, sputtering yields (γ) calculated by SRIM significantly deviate from the values deduced using the experimental measurements [45,46]. Here, we opt for an already developed approach of modifying SBE to minimize the difference between the γ values simulated by SRIM and the ones calculated using empirical equations derived from the experimental data [45] to be around 10% across the entire range of the Ar ion energies. For more details, please see Mahne *et al.* [47] and Farhadizadeh *et al.* [48]. The summary of the input parameters is provided in **Table S1** of the ESI.

The conclusion should be drawn with extra care, as SRIM/TRIM can underestimate the sputter yield at normal incidence and overestimate it for the glancing incidence [49]. However, this simple approximation suffices for our purposes.

2.4. An analytical model and numerical NP growth simulations

The MATLAB package was used to perform the simulations of a single Nb NP size growth, the NP temperature, and the Nb atomic deposition rate as functions of time-of-flight (the simulation scale is schematically shown in Fig. 1**c**). The approach to modeling the phenomena within our GAS is inspired by the work done by Zhao *et al.* [25] The model was modified to accommodate the influence of positive Ar ion bombardment and atomic sticking coefficient on the growth of NP. A more detailed description of the numerical calculations can be found in the ESI.

2.5. Equilibrium Nb NP shape (Wulff construct)

The equilibrium shape of Nb NPs was constructed using the

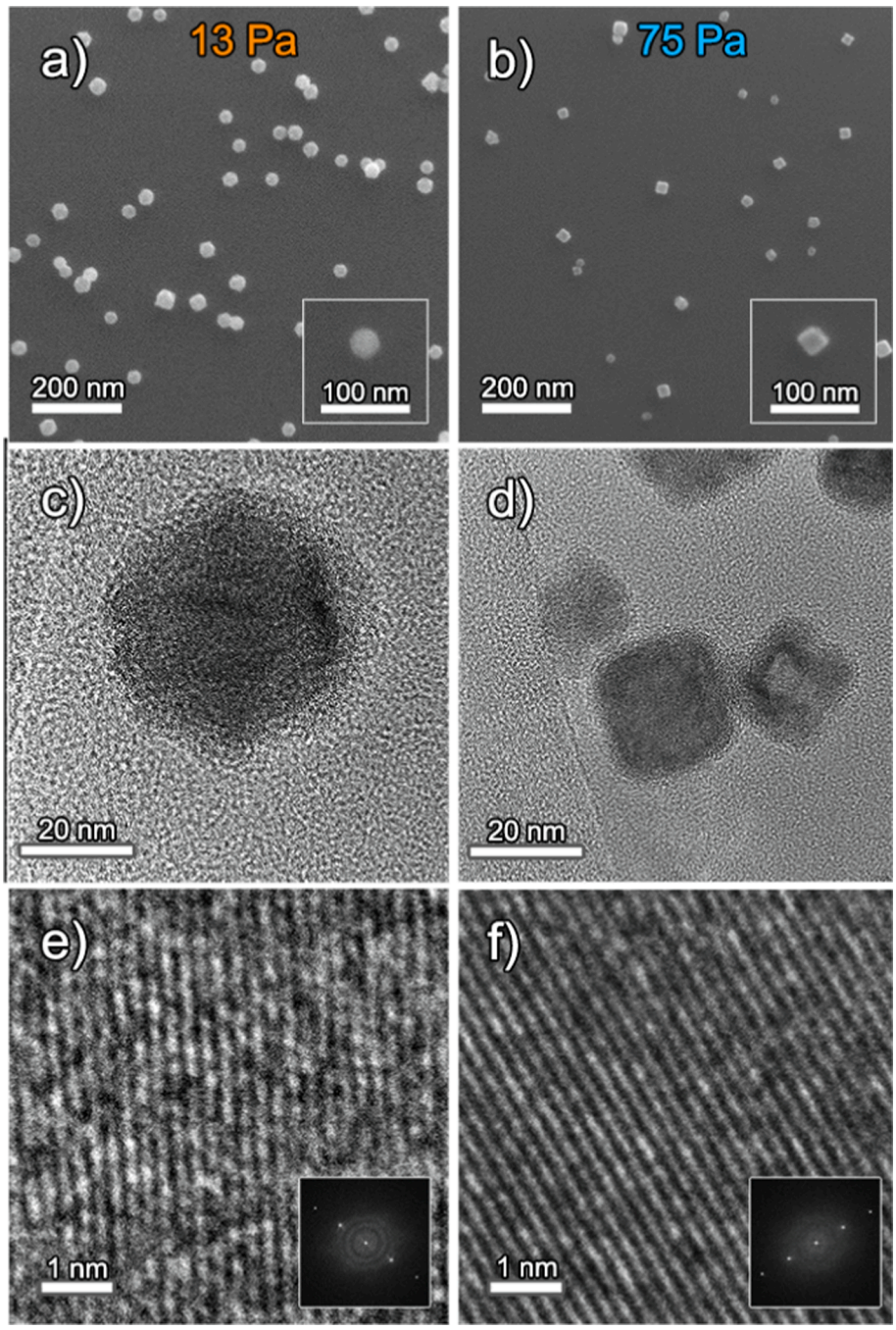

Fig. 2. Top view SEM (a, b) and HRTEM (c, d) micrographs of the Nb NPs synthesized at 13 Pa and 75 Pa of Ar pressure inside the aggregation chamber and constant current of 500 mA. The highly crystalline structure is shown on the HRTEM micrographs of bigger magnification (e, f). Insets show Fast Fourier Transform (FFT) images obtained on single NPs.

WulffPack software package [50,51]. An equilibrium shape of *bcc* Nb NP was modelled based on unit cell and lattice constant experimentally determined from XRD patterns as well as the set of facets with corresponding surface energies available in the literature [52–54]. The final structure included 50 000 Nb atoms. More details can be found in the ESI (**TableS2** and **Table S3**).

2.6. Molecular dynamics simulations of Nb NP growth

All molecular-dynamics simulations in this work were performed using classical molecular dynamics implemented in the LAMMPS code [55], with a time step of 1 fs. The Nb-Nb interactions were described by the EAM potential as fitted in [56]. The simulations took place in a cubic cell with periodic boundaries in all directions and started with an NP core of 27 atoms (1 nm size) in the middle of the cell. Such choice guarantees that NP core is significantly larger than a single Nb atom allowing to distinguish between the temperature of the NP and surrounding Nb atoms temperature and to bypass the complexity introduced by the quantum effects. On the other hand, 27-atom big core is still sufficiently small to affect the studied relationships between growth conditions and NP shape.

The NP temperature (T_{NP}) was controlled by a Nosé–Hoover thermostat (canonical *nvt* ensemble, asymptotical correction of the difference between actual and the target temperature) with a target temperature of 300–2200 K and a damping time of 20 fs. The temperature of Nb atoms not bonded to the NP was not controlled

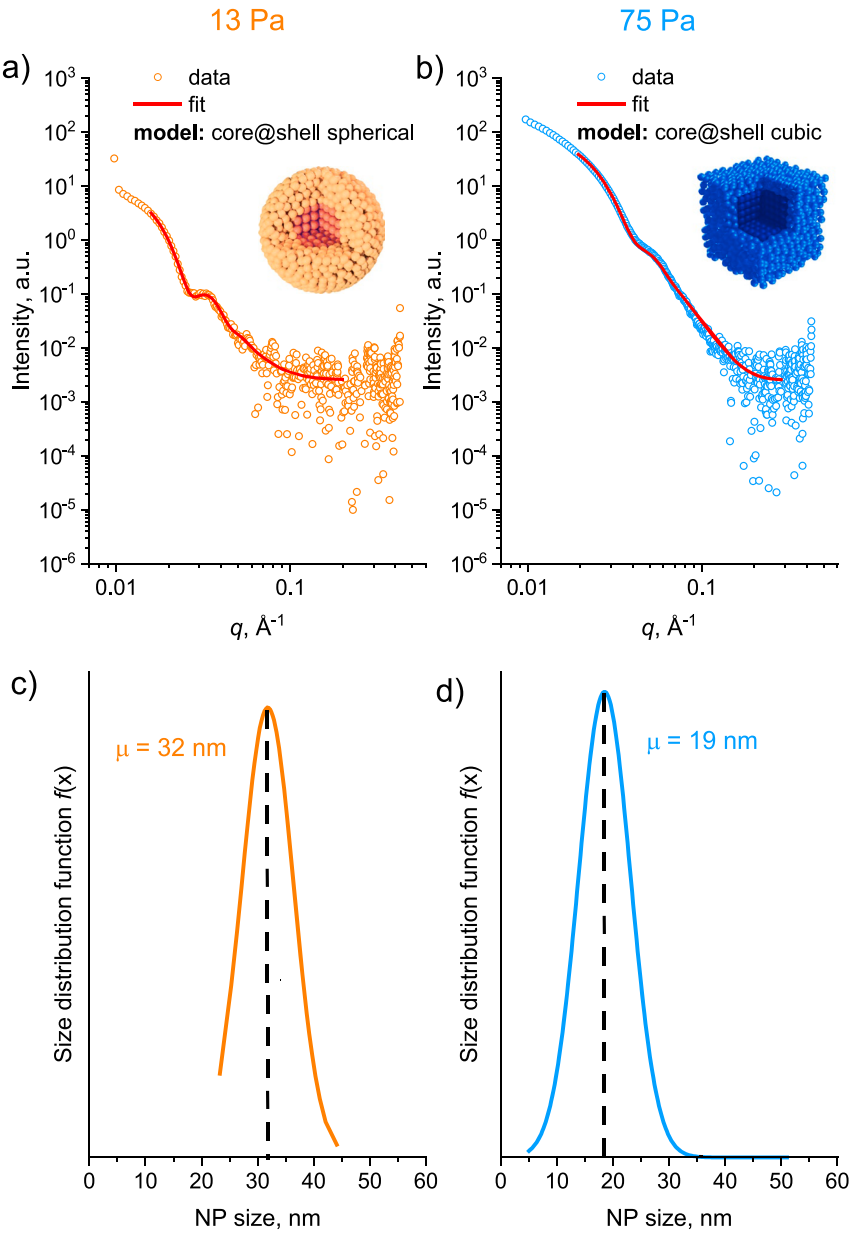

Fig. 3. Fitted SAXS scattering curves (a, b) and volume size distribution of Nb NPs (c, d) obtained from the fit of the SAXS data for the spherical NPs prepared at 13 Pa and cubic NPs prepared at 75 Pa and a constant current of 500 mA. The total size includes the metal core and 2-nm oxide shell.

(microcanonical *nve* ensemble). Two simulation protocols have been used for high and low Nb atom concentrations.

In the case of high Nb atom concentration simulations, the 10 × 10 × 10 nm cell was randomly filled with Nb and Ar atoms to a net concentration of 1 atom per 1 nm^3, with a minimum initial interatomic distance of 0.7 nm and with the atomic gas ratio R_g = Nb/(Nb + Ar) = 0.5. It should be recognized that such an unrealistically high Nb atom concentration was chosen to accelerate the simulations, but it significantly exceeds the real atomic vapor concentration in conventional magnetron sputtering. The Nb-Ar and Ar-Ar interactions were described by the Ziegler-Biersack-Littmark (ZBL) and Lennard-Jones potential, respectively. The NP growth via adsorption events was interrupted every 5 ps by introducing new Nb atoms and removing Ar atoms, in order to preserve both concentrations (taking the decreasing gas volume into account). Assuming that nucleation from hyperthermal atoms is unlikely, the highest initial temperature of the Nb atoms (T_{Nb}) was set at T_{Nb} = 2750 K (bulk Nb melting point). The temperature of the Ar atoms (T_{Ar}) was controlled at 300 K (corresponding to cooling at the GAS with water at room temperature).

In the case of low Nb atom concentration simulations, the 40 × 40 × 40 nm cell included the NP and a single arriving Nb particle with a random initial position above the NP surface and a random direction (but always intersecting the NP) of the initial velocity. The particle was either an isolated atom (T_{Nb} = 1600–2750 K) or a molecule containing up to 16 atoms (initial translational energy corresponding to T_{Nb} = 2750 K, with no initial vibrational or rotational energy). The time between two arrivals (except in simulations focused on its effect) was 1 ps. These simulations are similar to well-established growth simulations of metallic and other layers[57], except for the spherical instead of flat growth template used.

Although the NP can exist outside the range of temperatures chosen, extreme temperatures (far above T_{Nb}) cause the NP amorphization and, thus, lie beyond the region of interest for capturing phenomena that determine the NP morphology.

The medium-range order was quantified in terms of common neighbor statistics [58]. It counts triads *ijk,* where *i* is the number of

common neighbors of two bonded atoms, *j* is the number of bonds between these neighbors, and *k* is the maximum length of a chain made of these bonds. The *bcc* structure of Nb (assuming coordination of 14, i.e. bonds to first and second nearest neighbors) is characterized by 3 triads 444 + 4 triads 666 per atom, while e.g. icosahedra clusters which are of high importance in metallic glasses are characterized by triads 555.

2.7. Computational fluid dynamics simulations

The longitudinal pressure gradient across the aggregation chamber was modelled by computational fluid dynamics (CFD). The CFD simulations were performed for the 2D axisymmetric computational domain using the software Siemens STAR CCM + 16.06.008-R8 (double precision). The segregated fluid solver with Semi-Implicit Method for Pressure Linked Equations (SIMPLE) algorithm were used to numerically solve Navier-Stokes equations. A relatively low Knudsen number (K_n < 0.01) was set in fluid properties to allow for treating the carrier gas flow as a continuum. In the regions characterized by the transitional flow ($0.01 < K_n < 0.1$) the Maxwell slip corrections were applied. For CFD analysis, the following assumptions were made:

- Fluid was assumed to be ideal gas and to be compressible;
- No slip on the walls was expected, except for the regions with transitional Knudsen number (orifice, deposition chamber, etc.), where Maxwell partial slip model was used;
- Flow of the fluid was expected to be laminar;
- Polyhedral mesh was produced for this simulation;
- No electromagnetic interactions were considered the model.

3. Results and discussion

3.1. Morphology and structure of Nb NPs

Fig. 2 shows the SEM micrographs taken on the Nb NPs prepared at two different Ar pressures/flows in the aggregation chamber (13 Pa/2 sccm and 75 Pa/20 sccm), but with a constant current of 500 mA. At a low Ar pressure, most of the NPs are characterized by a close-to-spherical shape corresponding to the lowest surface-to-volume ratio. The increase in pressure triggers morphological changes and leads to more faceted NPs that become the dominant population. Here, a close-to-cubic symmetry is realized for most of the NPs. Hereafter, both types of NPs will be referred to as spherical and cubic for simplicity. For both cases, the HRTEM micrographs reveal that NPs are partially oxidized, demonstrating a polycrystalline metal core and a 2-nm thick niobium oxide shell formed as a result of NP oxidation upon exposure to the ambient atmosphere.

The observed morphological changes are accompanied by a nearly twofold decrease in the mean size of the NPs. Fig. 3 shows the SAXS scattering curves (a, b) and the NP size distributions (c, d). Considering the SEM/HRTEM results, the spherical and cubic core@shell models with 2-nm thick shells were chosen to fit the scattering curves. The best fit was obtained with the Gaussian size distribution function, characterized by the mean NP size μ of 32 nm for spherical (13 Pa) and 19 nm for cubic NPs (75 Pa), both including oxide shells (Fig. 3**c, d**). The results agree well with those obtained from the SEM images (**Figure S3**). The increase of Ar pressure in the aggregation chamber is also manifested by a change in the NP deposition rate (Fig. S2a) and the target bias tail-off (Fig. S2b).

The NP size decrease at high pressure (75 Pa) as compared to low pressure (13 Pa) might seem counter-intuitive because such outcome contradicts the expected NP growth owing to faster condensation rate facilitated by greater number of elastic collisions the growing NP experience with cooled buffer gas atoms. While the cooling rate by the buffer gas plays an important role, the NP final size is also affected by a miscellany of parameters and interplay between them. The NP residence time is one of such parameters.

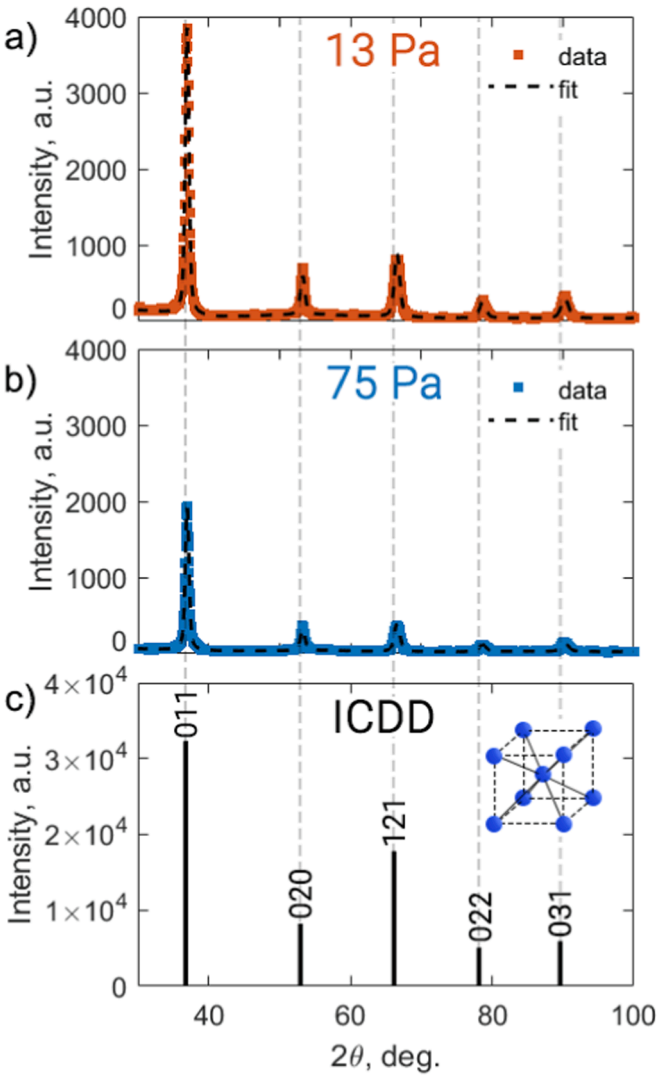

Fig. 4. X-ray diffraction patterns acquired on Nb NPs deposited at (a) 13 Pa and (b) 75 Pa. The data from the ICDD powder diffraction file (00–035-0789) are given for reference (c).

The NP residence time is defined as a NP time-of-flight inside the aggregation chamber, i.e. a time the NP actually spends inside that chamber. Under the assumptions that the Nb atom concertation in the gas phase is constant and the NP velocity is approximated by the linear velocity of the buffer gas flow, the NP residence time at higher pressure (75 Pa, 20 sccm) is about 2 times smaller as compared to that at smaller pressure (13 Pa, 2 sccm).

Such qualitative estimation is rather rough and does not reflect the fact that the sputtering yield is indirectly influenced by the gas flow. At higher gas flows (pressures), the energy distribution of impinging Ar ions shifts towards smaller energies because of more frequent collisions with neutrals. This is manifested via a decrease of sputtering yield (Fig. S2c) and, therefore, the Nb atom concertation in the gas phase. The lower concentration of metallic vapors also contributes to the smaller final NP size at high pressures.

Finally, the approximation of the NP by linear gas velocity is far from real scenario where the increase in the NP velocity with the pressure in the aggregation chamber could be up as big as 3 times as witnessed by the measurements carried out by our group on Cu NPs [59].

Despite the morphological changes, the Ar pressure in the aggregation chamber does not affect the NP crystallinity. The Nb NPs prepared at 13 Pa and 75 Pa produce nearly identical XRD patterns, as shown in

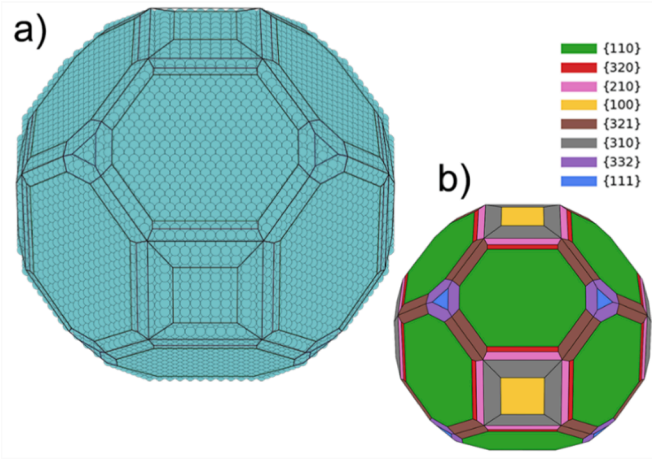

Fig. 5. The theoretical equilibrium shape of bcc Nb NP: a) atomistic view, b) surface view.

Fig. 4. According to the data from the ICDD powder diffraction file (00–035-0789), the Nb NPs consist of a body-centered cubic phase (space group 229). This correlates well with our earlier findings on magnetron-sputtered Nb NPs [17,41]. The acquired XRD patterns were fitted to extract the parameters of the Nb *bcc* phase. The lattice constant is found to remain the same (3.4398(4) Å) for the Nb NPs prepared at 13 Pa and 75 Pa of Ar pressure. The measured value is found to be larger by a few percent than that of bulk niobium. Such discrepancy is caused by the surface oxidation of Nb NPs [60].

3.2. Equilibrium shape of Nb NPs

The magnetron-sputtered NP are predominantly characterized by polyhedral shapes with some degree of truncation. The occurrence of a particular shape is often related either to growth rates that are highly dependent on crystal orientation or to surface energy minimization processes. In the latter case, the Wulff construction provides a simple, yet powerful method for the prediction and analysis of the equilibrium shape of nanoparticles. The NP shape is governed by the surface energies of the material [51] calculated using *ab initio* methods. We take advantage of the Wulff construction method to simulate an equilibrium shape of a Nb NP which is dependent on a number of exposed facets as well as free surface energies thereof [52–54]. Such an approach provides a point-of-reference.

Fig. 5 shows the shape of a single Nb NP when it is formed under equilibrium conditions. The largest surface areas of the metal are presented by {1 1 0} and {1 0 0} facets. On the other hand, high-index facets such as {3 1 0} and {3 2 1} also contribute to the net surface. The Wulff-constructed shape confirms that Nb, similar to some other transition metals, tends to evolve into a multifaceted, close-to-spherical shape when driven purely by energy minimization processes. However, such reasoning alone does not explain the observed differences in the experimental data. Although NPs retain overall crystallinity for high operational pressures, they form cubic shapes.

3.3. Molecular dynamics simulations

To gain insight into the formation of different NP shapes, we employed molecular dynamics simulations. The results of the high Nb atom concentration simulation show that either amorphous or crystalline NPs can be formed, depending on the NP temperature. At a higher T_{NP}, no ordering can be found in the NP structure (Fig. 6**a**). The NP is essentially amorphous and retains spherical symmetry. However, at a lower T_{NP}, the Nb atoms rearrange themselves to form a distinct crystalline order (Fig. 6**b**). The NP shows signs of faceting, although a

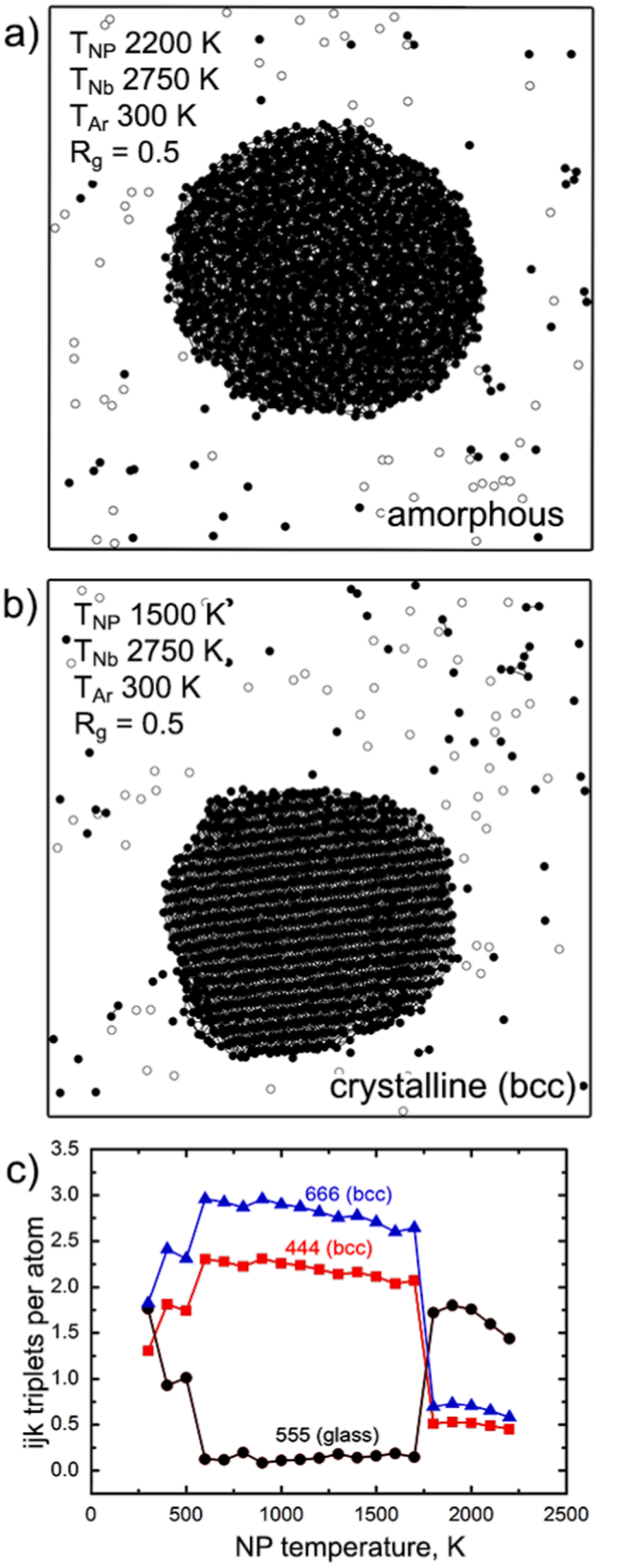

Fig. 6. MD simulations of high Nb atom concentration: slices of the Nb NPs grown in the simulation cell at R_g = Nb/(Ar + Nb) = 0.5, T_{Nb} = 2750 K, T_{Ar} = 300 K and different T_{NP}: a) 2200 K and b) 1500 K (solid black symbols are Nb atoms, open white symbols are Ar atoms); c) common neighbor statistics at different T_{NP} and T_{Nb} = 2750 K.

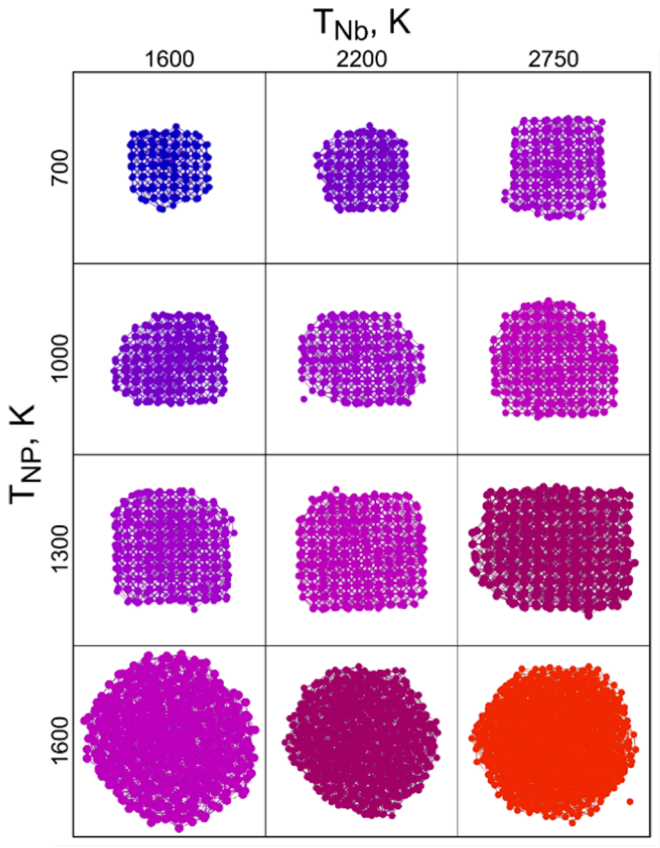

Fig. 7. Low Nb atom concentration (atom-by-atom growth) MD simulations: snapshots (slices) of the Nb NP grown in the simulation cell at various T_{Nb} and the T_{NP} temperatures. The simulation time is 5000 arrivals.

distinct cubic shape is not achieved.

The network topology (common neighbor statistics) was calculated for the range of T_{NP} and the results are shown in Fig. 6**c**. For certain growth conditions, the common neighbor statistics are closer to *bcc* (*ijk* = 444 and 666), if one considers both the first and second nearest neighbors in *bcc* (coordination of 14, not 8), whereas for other conditions, the common neighbor statistics exhibit a lot of triplets 555 characteristic of metallic glasses (amorphous phase). For the high NP temperature range ($T_{NP} > 1700$ K), the incoming Nb atoms do not lose sufficient energy to form an ordered lattice and remain in a disordered state; the amorphous phase dominates in this case. At a T_{NP} of about 1700 K, a sudden crossover is observed: the Nb atoms start dissipating their energy upon their interaction with the atoms of the condensed phase, yet staying sufficiently mobile to arrange themselves into a highly ordered lattice. Here, the contribution of the amorphous phase is negligible. At $T_{NP} < 600$ K, the NPs again lose their crystallinity, and the amorphous phase takes over. We attribute this effect to the fast thermalization of the incoming Nb atoms on a cold condensed phase. Fast thermalization favors the retention of the atomic-scale disorder given by the temporal and spatial randomness of the arrival of Nb atoms. Because the experiments did not produce Nb NPs in the glassy state, we can consider fast NP cooling unlikely in our case.

To investigate the influence of T_{Nb} and T_{NP} on the resultant NP structure under closer-to-reality conditions, MD simulations were performed in an atom-by-atom adsorption regime (**Figure S4**). In contrast to the above simulations, the cell with an initial 1 nm-sized NP was not filled with the Nb/Ar mixture, but the Nb atoms were introduced into the cell one by one from random directions with a frequency of 1 atom per 1 ps. Ar atoms were not introduced at all, but they were implicitly present as a tool to control the energy of the arriving Nb atoms. Thus, a lower T_{Nb} implies that Nb atoms lost part of their momentum in collisions with Ar atoms. The approach allowed us to simulate the situation of typical magnetron sputtering under which the concentration of metal atoms is much smaller than that of Ar.

Fig. 7 shows the slices of the NPs produced at different T_{Nb} and T_{NP}. Similar to previous findings, high T_{NP} results in the growth of amorphous NPs. These NPs are characterized by a close-to-spherical shape that does not depend on the temperature of the incoming Nb atoms. Although the crossover to the crystalline morphology occurs at somewhat lower $T_{NP} < 1600$ K, the same trend holds: NPs with the *bcc* structure are formed at lower values of T_{NP}. In contrast to the high-concentration simulations, these NPs are more distinctly faceted and, in some cases, provide rectangular cross-sections remarkably resembling the cubic projections found in the HRTEM micrographs.

Metal sputtering is generally regarded as an atomistic process, although the ejection of dimers and higher mers from the target is also possible [61,62]. Either originating from the target or from the gas-

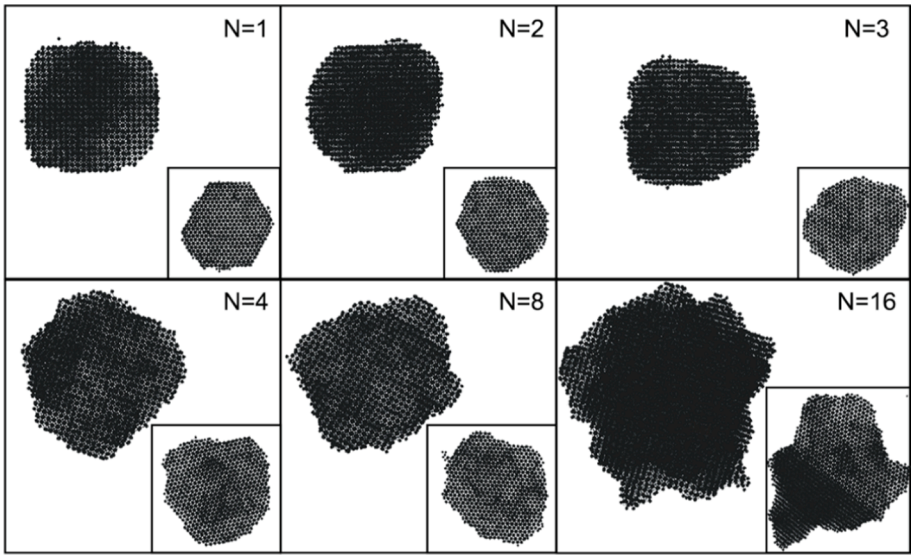

Fig. 8. Low-Nb-atom-concentration (atom-by-atom) MD simulations: snapshots (slices) of Nb NPs grown from different 'precursors': N = 1 denotes a single Nb atom, N = 2 – Nb dimer, N = 3 – Nb trimer, etc. The T_{NP} and the T_{Nb} are 1000 K and 2750 K, respectively. Snapshots are chosen to show NPs of approximately the same size. Inset in each panel corresponds to the same NP viewed from a different direction.

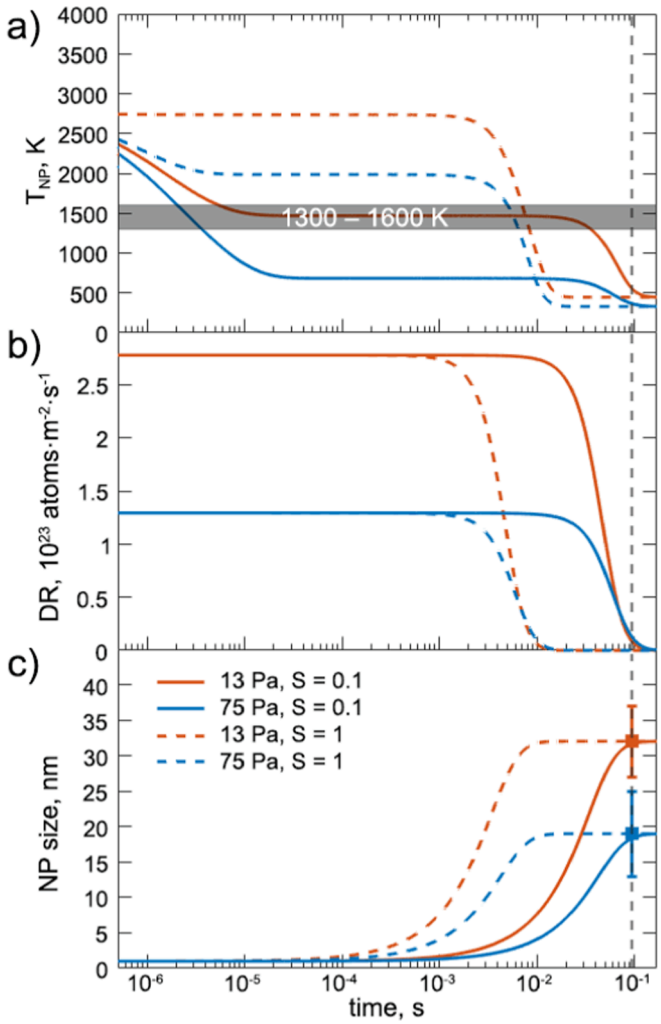

Fig. 9. Time evolution of: a) the NP size; b) the NP temperature, and c) Nb atomic deposition rate for Ar pressure of 13 Pa and 75 Pa in the aggregation chamber and sticking coefficient values of 0.1 ($S = 1$ is also shown for reference). The initial temperature of a Nb seed (29 atoms) is set to 2750 K. The horizontal patterned box at $T_{NP} = 1300$—1600 K corresponds to the amorphous-crystalline transition range obtained from the atom-by-atom MD simulations. The magnetron current is 500 mA. The symbols in the top right corner correspond to the mean Nb NP size obtained experimentally. The scatter points with error bars correspond to the NP size distributions extracted with SAXS. The vertical dashed line corresponds to the approximate distance of 10 mm. The spatial scale corresponds to the distance of 0.3 to 15 mm from the magnetron target.

phase reactions, diatomic molecules of metals are not stable in the plasma and have a high probability of undergoing disintegration. In terms of NP synthesis, the disintegration of dimers is an undesirable process because they may serve as nucleation seeds and facilitate the formation of NPs. Nb is remarkable in this sense because, as a refractory metal, it possesses high cohesive energy. For example, the dissociation energy of Nb_2 exceeds 5 eV [63] and, therefore, these dimers are expected to survive the plasma conditions more efficiently [64].

We applied the MD simulations to investigate the possible contribution of diatomic and multiatomic Nb species to the NP growth. Similar to Fig. 7, the simulations were performed in the low atomic concentration regime in which the Nb_N species ($N = 1$–16) are introduced into the cell one by one at a frequency of 1 species per 1 ps. The T_{NP} was set at 1000 K (~middle of the temperature range that led to crystallinity in the previous simulations), while the T_{Nb} was set at 2750 K. The initial velocity of all atoms in the precursor was the same (i.e. all initial energy was in the translational degrees of freedom, not in rotational and vibrational). Fig. 8 shows that the shape of the NPs strongly depends on the type of "precursor", either a single atom, dimer, trimer, etc. The NPs become less faceted and acquire irregular shapes when they grow from the larger *N*-mers. We attribute this effect to the difference in the sticking efficiency between single Nb atoms and Nb_N species. The sticking coefficient was found to be 0.14 for single atoms, whereas it increases dramatically to > 0.90 for the *N*-mers. Thus, single atoms adhere to the NP in an attachment-limited aggregation regime [65] which is known for producing NPs of close to spherical shape. In contrast to that, a higher probability of sticking results in the development of a ramified morphology. This was earlier exemplified by an extreme type of diffusion-limited aggregation with the sticking coefficient of 1 that produced dendritic NPs. [66,67] Since no such NPs were experimentally observed, we conclude that Nb_N species do not play a significant role in the sputter-driven NP growth, and this growth is driven predominantly by the accretion of single Nb atoms. Furthermore, MD simulations with the different time between two atomic arrivals showed that the resultant NP morphology does not depend on the arrival frequency (**Figure S5**). Therefore, the rate with which Nb NPs arrive at the surface of the growing NP (the atomic deposition rate) does not influence the resultant NP shape.

3.4. An analytical model and numerical calculations of Nb NP growth

The current paradigm of gas-phase growth of metal NPs considers the formation of an embryo in the transition (excited) state. When a newly arrived atom is adsorbed, the condensation energy is released and

dissipated among the vibrational degrees of freedom of atoms constituting the embryo, thus increasing the temperature of the growing NP. At the same time, the NP loses energy through interaction with cold Ar atoms as well as via black body radiation. The overall thermal kinetics determines *inter alia* the resultant crystallinity of the NPs.

A state-of-the-art analytical model of Zhao [25] (based also on the earlier observations of Westergren) [68] has considered the above energy gain and loss channels and offered tools to assess the evolution of the NP size and temperature (T_{NP}) in time. Going beyond the state-of-the-art, one may notice that sputter-based gas aggregation of NPs proceeds in space where low-temperature plasma is present. Non-equilibrium conditions in such plasmas differ significantly from the conditions of conventional gas-phase condensation: for example, hyperthermal ion and electron bombardment should also be considered as an additional channel for heating NPs bearing negative and positive charges. For NPs of several nanometers in size and larger, we simplify the problem by idealistically neglecting fluctuations of charge signs [69] and assuming that all NPs bear a single negative charge in the plasma, undergoing the bombardment from positively charged Ar^+ ions. A new term is introduced to the Zhao model to account for such ion-driven heating.

Another factor in play, which is often neglected, is an atomic sticking coefficient S, which represents the ratio of the number of deposited atoms to the number of impinging atoms. We consider a situation when no energy barriers are imposed, that is S is close to unity at low surface temperature and it decreases with increasing $T_{surface}$. In practice, however, S could be strongly affected by many other factors, such as crystal orientation and surface roughness [25,30]. Without knowing the temperature dependence of S for Nb, we simplify this problem by assuming that S remains constant during NP growth, performing calculations for $S = 0.1$ (which is close to the value of 0.14 obtained from the MD simulations). We also show the results for $S = 1$ chosen as the maximum possible, but less realistic value.

The model omits the nucleation phenomena and considers an already existing NP with an initial temperature of 2750 K ($T_{init} = T_{melt}$ of bulk Nb) and the number of atoms 29 (corresponding to an NP of 1 nm size). Such NP grows via the deposition of thermalized Nb atoms coming from the gas phase. In general, the NP heats up as latent heat is released upon Nb atom attachment and cools down through interactions with ambient Ar atoms as well as via black-body radiation. To describe the simultaneous temporal evolution of NP size, temperature and atomic flux (that is, the number of Nb atoms deposited per area unit per time), we can modify Zhao's system of differential equations as follows:

$$\begin{cases} \dfrac{dN(t)}{dt} = S\pi r_{NP}^2\left(n_{Nb} - \dfrac{N(t)}{V}\right)\upsilon_{Nb} \\ \dfrac{dT(t)}{dt} = \dfrac{\pi r_{NP}^2}{3k_B N(t)}\left[3k_B(n_{Ar} - n_{Ar+})\upsilon_{Ar}(T_{Ar} - T(t)) + 2n_{Ar+}\upsilon_{Ar+}E_{Ar+} + S2\left(n_{Nb} - \dfrac{N(t)}{V}\right)\upsilon_{Nb}E_{co}\right] - \dfrac{8\pi r_{NP}^2\sigma\epsilon(T(t)^4 - T_{Ar}^4)}{(3k_B N(t))} \end{cases}$$

cooling by Ar *heating by Ar^+* *heating by Nb* *cooling by radiation*

Here, a new term $2n_{Ar+}v_{Ar+}E_{Ar+}$ was introduced to account for the heating due to the ion bombardment, while the deposition rate and the heating due to the adsorption of Nb atoms were modified by introducing the sticking coefficient. A more detailed description of the analytical model can be found in the Electronic Supplementary Information.

The results of the numerical solutions are presented in Fig. 9 for the Ar pressure of 13 Pa and 75 Pa and $S = 0.1$ (for comparison, $S = 1$ is also shown). The time scale was chosen from 10^{-6} s to 0.5 s, which corresponds to the distance from 0.3 to 15 mm from the magnetron under the assumption that NPs travel along the aggregation chamber with the linear velocity of Ar. The lower limit was chosen based on the mean free path that reaches 0.25 mm for 13 Pa. Below that value, the atomic collisions are less frequent, and the existence of nanometer-sized NPs is not expected. The higher boundary was chosen to go beyond 10 mm, which corresponds to the approximate propagation of the plasma zone above the target.

The NPs grow under three different temperature regimes that can be distinguished in Fig. 9: 1) early cooling; 2) steady-state; 3) late cooling.

1) Early cooling ($<10^{-5}$ s).

Since the analytical model does not consider nucleation phenomena and starts with an already existing 1-nm-sized NP, its initial temperature should be chosen. For the calculations, the initial T_{NP} was set at 2750 K, the melting point of Nb. Starting from this temperature, the NPs cool down, and the lower-pressure conditions demonstrate a slower fall of the temperature curve. Thus, NPs cool slower at 13 Pa and faster at 75 Pa. For later reference, it can be noted that T_{NP} reaches ~ 1500 K for 13 Pa, which is close to the upper limit of the temperature range of the phase transition between the crystalline and amorphous state found by the MD simulations. For 75 Pa, T_{NP} decreases to ~ 700 K, which is below this phase transition. The atomic deposition rate is significantly higher for 13 Pa, reflecting a higher sputtering yield at a lower pressure (this correlates well with the SRIM/TRIM simulations shown in the Electronic Supplementary Information). Thus, the higher T_{NP} attained for 13 Pa can be explained by a less efficient NP cooling via collisions with Ar atoms and by a more efficient NP heating due to the higher flux of Nb atoms. On the contrary, higher Ar pressures hinder the arrival of Nb atoms and provide faster NP cooling via collisions with Ar atoms, resulting in lower T_{NP}. Regardless of Ar pressure, no substantial growth of NPs is observed on this time scale of $< 10^{-4}$ s.

2) Steady-state ($10^{-5} - 10^{-2}$ s).

This is an intermediate stage of the growth process, in which the atomic deposition rate is constant, energy gains and losses become balanced, the NP temperature also stays at a constant level, and the NPs grow in a steady-state temperature regime. As noted above, at Ar pressure of 13 Pa, T_{NP} stays close to the upper limit of the phase transition between the crystalline and amorphous state. Hence, the Nb NPs remain amorphous when they grow in the lower-pressure plasma. It is worth noting that such conditions lead to NP growth to the spherical shape. In contrast, at 75 Pa of Ar pressure, the NPs grow at a temperature below the phase transition, leading to the formation of the faceted morphology.

3) Late cooling ($>10^{-2}$ s).

At the time $> 10^{-2}$ s, the atomic deposition rate starts to decrease abruptly. Energy losses dominate over the energy gains, and the NPs start to cool down again. In contrast to the early stage, cooling is faster for 13 Pa due to a steeper decrease in the atomic deposition rate; nevertheless, maximal cooling rates are of the same order of ~ 10^4 K/s for both pressures. Such rates are far below 10^{12} K/s required for single-element metals to arrest the structure in the glassy state,[70,71] and the phase transition from the amorphous to the crystalline state occurs for

13 Pa, leading to the formation of the *bcc* lattice. However, the final NP shape is different for the two pressures in question. Previous reports showed that a cubic or spherical shape can be realized depending on the competition between the atomic flux onto the NP surface and the atomic diffusion over the NP surface. Given this paradigm, we may estimate the frequency of the atomic arrivals from the atomic flux and the NP surface area as $\sim 10^8$ Hz. The frequency of the diffusion attempts was determined earlier as $\sim 10^{12}$ Hz for Nb self-diffusion at similar temperatures [72]. The comparison shows that the atomic deposition rate is low and does not restrict surface diffusion for any of the pressures.

For the low atomic deposition rate, if the diffusion barriers at different lattice planes are close (as is the case for T_{NP} close to the melting point), the NPs maintain the spherical shape because all of the diffusion directions are equally probable. However, at lower T_{NP}, the difference between the diffusion barriers becomes large, determining lattice planes with hindered and preferential surface diffusion. As a consequence, the cubic morphology evolves for *bcc* metals [25].

Here, Nb NPs cool from significantly different T_{NP} at different pressures. For a low pressure of 13 Pa, the T_{NP} decreases from $\sim$ 1500 K, and these NPs pass through the amorphous-to-crystalline transition region at the moment when they have already grown to spheres of 30 nm, which is close to their final size of 32 nm. After crystallization, diffusion-limited faceting comes into play, but the remaining atomic flux is almost exhausted and insufficient to complete the cubic morphology. For 75 Pa, the NPs proceed to grow retaining the cubic morphology.

At a distance of $\sim$ 10 mm from the target, the NPs leave the plasma and enter the afterglow. Here, the growth has already been completed and the NPs have acquired the final size. However, the NPs are still hyperthermal: a lower pressure of 13 Pa leads to worse cooling and a higher $T_{NP} = 570$ K, whereas the higher pressure is more cooling efficient, resulting in a lower $T_{NP} = 370$ K. Therefore, depending on the pressure, Nb NPs can be 'hot' when they leave the plasma. This finding is consistent with our recent investigations of the energy flux brought from the plasma to the afterglow during the formation of Cu and W NPs [73]. The energy flux was found to be substantial in this region, although it decreased rapidly at further distances from the plasma. Under identical conditions, the energy flux for W was found to be three times that of Cu, which was given mainly by the much higher cohesion energy of the former.[74] As the cohesion energy of Nb is close to that of W, we can expect that its contribution to the energy balance is highly important and, together with the sputtering parameters, determines the kinetics of the cooling and shape formation of Nb NPs.

It should be explicitly stated that the above calculations need to be interpreted with care because of the simplifications made. For example, Fig. 9 shows the same dependencies calculated with $S = 1$. Although qualitatively the same three stages are reproduced, the time scales and, more importantly, the temperature range are different. For both pressures, the NPs remain in the liquid state far beyond the crystallization temperature until the very late stage of $t > 10^{-2}$ s. This behavior seems to be unlikely as it assumes an ideal sticking, contradicts the MD simulations, and does not explain the spherical/cubic morphology obtained at different pressures. However, due to a non-constant sticking coefficient obeying the temperature function of an unknown form, the real dependencies of Fig. 9 may be affected in an unpredictable way, and further research is needed.

4. Conclusions

Niobium NPs can be synthesized by dc magnetron sputter-based gas aggregation, with their morphology tuned in dependence on the Ar pressure in the aggregation chamber. Close-to-spherical NPs are formed at a lower Ar pressure of 13 Pa, and cubic NPs are formed at a higher Ar pressure of 75 Pa. Spherical NPs grow to a larger mean size of 32 nm, whereas cubic NPs have a smaller size of 19 nm. Regardless of the pressure, Nb NPs retain the same body-centered cubic structure (space group 229).

MD simulations show that NP growth proceeds via the adsorption of single Nb atoms and not via dimers, trimers, or heavier species. The sticking coefficient of atomic Nb to Nb NPs is found to be 0.14. It is also found that the NP temperature should be in the 600 – 1700 K range during growth to ensure the formation of the *bcc* lattice with the faceted morphology; otherwise, the NPs remain amorphous and retain spherical symmetry. The energy and flux of incoming Nb atoms do not influence either the resultant crystallinity or the NP shape.

Zhao's analytical model of energy gain and loss during NP growth was modified to account for the energy gain from Ar ion bombardment in the plasma and the energy loss due to non-ideal atomic sticking. The modified model demonstrates that, at a lower pressure, the NPs remain at a temperature higher than the amorphous-to-crystalline phase transition because of inefficient cooling by Ar atoms. Therefore, they grow in a glassy state under the conditions of isotropic surface diffusion, resulting in the spherical shape of NPs. For higher pressure, the NP temperature is lower than that of the phase transition because of more efficient cooling. The NPs crystallize into a *bcc* structure and their growth proceeds with different diffusion barriers in different atomic planes, defining the cubic shape.

During the transition from the plasma to the afterglow, NPs start thermalizing because of a drastic decrease of the Nb atomic flux arriving onto the NP surface. Thermalization proceeds at a comparable cooling rate of $\sim 10^4$ K/s for both pressures. For lower pressure, such a rate is not sufficient to retain the NPs in the glassy state, and they also crystallize into the *bcc* structure. However, by the time of the phase transition, the NPs have already grown to 85% of their final size, and insignificant growth below the phase transition temperature is not sufficient to form a faceted morphology in this case. For higher pressure, the NPs are already crystalline and their thermalization is accompanied by the growth with different diffusion barriers in different atomic planes, which define the final cubic shape.

Our analytical model highlights the sticking coefficient as one of the major factors that determine the kinetics of the NP growth and thermalization. Non-ideal sticking significantly affects the temperature regimes and the time scale at which the NPs grow. The model still fails to account for the non-constant temperature dependence of the sticking coefficient, which remains unknown and signals the need for additional studies.

Author Contributions

The manuscript was written through contributions of all authors. All authors have given approval to the final version of the manuscript.

Funding Sources

The grants GACR 21-12828S and GACR 19-14011S from the Czech Science Foundation.

The grant e-INFRA CZ project (ID:90254) from the Ministry of Education, Youth and Sports of the Czech Republic.

The grant CZ.02.1.01/0.0/0.0/15_003/0000485 from the European Regional Development Fund (ERDF).

CRediT authorship contribution statement

Pavel Pleskunov: Conceptualization, Methodology, Investigation, Validation, Formal analysis, Supervision, Software, Writing – original draft, Writing – review & editing, Project administration. **Tereza Košutová:** Investigation, Methodology, Formal analysis, Data curation, Visualization, Validation, Writing – original draft, Writing – review & editing. **Mariia Protsak:** Data curation, Formal analysis. **Marco Tosca:** Investigation, Formal analysis. **Kateryna Biliak:** Data curation. **Daniil Nikitin:** Investigation. **Zdeněk Krtouš:** Investigation, Software, Visualization. **Jan Hanuš:** Investigation, Formal analysis, Validation. **Jiří Houška:** Investigation, Methodology, Validation, Visualization,

Resources, Software, Writing – original draft, Writing – review & editing, Funding acquisition. **Miroslav Cieslar:** Investigation, Formal analysis, Validation. **Suren Ali-Ogly:** Investigation, Software, Formal analysis, Validation. **Peter Kuš:** Investigation. **Ondřej Kylián:** Conceptualization, Methodology, Resources, Supervision, Writing – original draft. **Andrei Choukourov:** Conceptualization, Methodology, Validation, Formal analysis, Resources, Supervision, Writing – original draft, Writing – review & editing, Funding acquisition, Project administration.

Declaration of Competing Interest

The authors declare that they have no known competing financial interests or personal relationships that could have appeared to influence the work reported in this paper.

Data availability

Data will be made available on request.

Acknowledgements

The work was supported via the grant GACR 21-12828S from the Czech Science Foundation. J.H. would like to acknowledge the support of MD simulations from the Czech Science Foundation under the grant GACR 19-14011S. Computational resources for numerical simulations were provided by the e-INFRA CZ project (ID:90254), supported by the Ministry of Education, Youth and Sports of the Czech Republic. The SAXS and XRD measurements were supported by ERDF in the frame of the project NanoCent - Nanomaterials Centre for Advanced Applications (Project No. CZ.02.1.01/0.0/0.0/15_003/0000485).

Appendix A. Supplementary material

Numerical NP growth simulations description; deposition rate of the Nb NPs measured by QCM, target bias voltage and sputtering yield (γ) calculated by SRIM/TRIM as a function of Ar pressure in the aggregation chamber; size distributions of Nb NPs calculated based on SEM micrographs; low atom density MD simulations; snapshots (slices) of the Nb NP grown in the simulation cell at various time intervals between arriving Nb atoms. Supplementary data to this article can be found online at https://doi.org/10.1016/j.apsusc.2023.158235.

References

[1] J.E. Greene, Review Article: Tracing the recorded history of thin-film sputter deposition: From the 1800s to 2017, J. Vac. Sci. Technol. A Vacuum, Surfaces, Film. 35 (2017) 05C204, https://doi.org/10.1116/1.4998940.
[2] J.A. De Toro, P.S. Normile, C. Binns, Types of Cluster Sources, in: Gas-Phase Synth. Nanoparticles, 2017: pp. 39–55. doi:https://doi.org/10.1002/9783527698417.ch3.
[3] H. Haberland, M. Karrais, M. Mall, Y. Thurner, Thin films from energetic cluster impact: A feasibility study, J. Vac. Sci. Technol. A Vacuum, Surfaces, Film. 10 (1992) 3266–3271, https://doi.org/10.1116/1.577853.
[4] H. Haberland, M. Mall, M. Moseler, Y. Qiang, T. Reiners, Y. Thurner, Filling of micron-sized contact holes with copper by energetic cluster impact, J. Vac. Sci. Technol. A Vacuum, Surfaces, Film. 12 (1994) 2925–2930, https://doi.org/10.1116/1.578967.
[5] J.T. Gudmundsson, Physics and technology of magnetron sputtering discharges, Plasma Sources Sci. Technol. 29 (2020), https://doi.org/10.1088/1361-6595/abb7bd.
[6] D. Llamosa, M. Ruano, L. Martínez, A. Mayoral, E. Roman, M. García-Hernández, Y. Huttel, The ultimate step towards a tailored engineering of core@shell and core@shell@shell nanoparticles, Nanoscale 6 (2014) 13483–13486, https://doi.org/10.1039/c4nr02913e.
[7] P. Mukherjee, B. Balamurugan, J.E. Shield, D.J. Sellmyer, Direct gas-phase formation of complex core-shell and three-layer Mn-Bi nanoparticles, RSC Adv. 6 (2016) 92765–92770, https://doi.org/10.1039/c6ra15799h.
[8] J.G. Mattei, P. Grammatikopoulos, J. Zhao, V. Singh, J. Vernieres, S. Steinhauer, A. Porkovich, E. Danielson, K. Nordlund, F. Djurabekova, M. Sowwan, Gas-Phase Synthesis of Trimetallic Nanoparticles, Chem. Mater. 31 (2019) 2151–2163, https://doi.org/10.1021/acs.chemmater.9b00129.
[9] R. Cheula, M. Maestri, G. Mpourmpakis, Modeling Morphology and Catalytic Activity of Nanoparticle Ensembles under Reaction Conditions, ACS Catal. 10 (2020) 6149–6158, https://doi.org/10.1021/acscatal.0c01005.
[10] A. Bayles, S. Tian, J. Zhou, L. Yuan, Y. Yuan, C.R. Jacobson, C. Farr, M. Zhang, D. F. Swearer, D. Solti, M. Lou, H.O. Everitt, P. Nordlander, N.J. Halas, Al@TiO2Core-Shell Nanoparticles for Plasmonic Photocatalysis, ACS Nano 16 (2022) 5839–5850, https://doi.org/10.1021/acsnano.1c10995.
[11] J. Lee, C. Jeong, T. Lee, S. Ryu, Y. Yang, Direct Observation of Three-Dimensional Atomic Structure of Twinned Metallic Nanoparticles and Their Catalytic Properties, Nano Lett. 22 (2022) 665–672, https://doi.org/10.1021/acs.nanolett.1c03773.
[12] A. Behera, Chapter 13 - Shape-controlled metal nanoparticles for fuel cells applications, in: H. Song, T.A. Nguyen, G.B.T.-N. in F.C. Yasin (Eds.), Micro Nano Technol., Elsevier, 2022: pp. 349–360. doi:https://doi.org/10.1016/B978-0-323-85727-7.00014-X.
[13] M. Kumar, J. Dey, S. Swaminathan, M. Chandra, Shape Dependency of the Plasmon-Exciton Interaction at the Nanoscale: Interplay between the Plasmon Local Density of States and the Plasmon Decay Rate, J. Phys. Chem. C (2022), https://doi.org/10.1021/acs.jpcc.2c00701.
[14] J. Kim, H. Hilal, M.N. Haddadnezhad, J. Lee, W. Park, W. Park, J.W. Lee, I. Jung, S. Park, Plasmonic All-Frame-Faceted Octahedral Nanoframes with Eight Engraved Y-Shaped Hot Zones, ACS Nano 16 (2022) 9214–9221, https://doi.org/10.1021/acsnano.2c01543.
[15] E. Elliott, K. Bedingfield, J. Huang, S. Hu, B. De Nijs, A. Demetriadou, J. J. Baumberg, Fingerprinting the Hidden Facets of Plasmonic Nanocavities, ACS Photonics 9 (2022) 2643–2651, https://doi.org/10.1021/acsphotonics.2c00116.
[16] J. Son, G.H. Kim, Y. Lee, C. Lee, S. Cha, J.M. Nam, Toward Quantitative Surface-Enhanced Raman Scattering with Plasmonic Nanoparticles: Multiscale View on Heterogeneities in Particle Morphology, Surface Modification, Interface, and Analytical Protocols, J. Am. Chem. Soc. (2022), https://doi.org/10.1021/jacs.2c05950.
[17] P. Pleskunov, V. Prysiazhnyi, D. Nikitin, T. Košutová, M. Cieslar, I. Gordeev, Z. Krtouš, S. Ali-Ogly, J. Šomvársky, M. Protsak, K. Biliak, K. Kishenina, A. Bednařík, M. Dopita, J. Preisler, A. Choukourov, Magnetron-Sputtered Niobium Nanoparticles for Molecular Imaging of Brain Tissues through Surface-Assisted Laser Desorption/Ionization Mass Spectrometry, ACS Appl. Nano Mater. 5 (2022) 12865–12875, https://doi.org/10.1021/acsanm.2c02734.
[18] M. Zhou, C. Li, J. Fang, Noble-Metal Based Random Alloy and Intermetallic Nanocrystals: Syntheses and Applications, Chem. Rev. 121 (2021) 736–795, https://doi.org/10.1021/acs.chemrev.0c00436.
[19] P.Z. Chen, A. Skirzynska, T. Yuan, O. Voznyy, F.X. Gu, Asymmetric Interfacet Adatom Migration as a Mode of Anisotropic Nanocrystal Growth, J. Am. Chem. Soc. 144 (2022) 19417–19429, https://doi.org/10.1021/jacs.2c07423.
[20] G.A. Drake, L.P. Keating, M. Shim, Design Principles of Colloidal Nanorod Heterostructures, Chem. Rev. (2022), https://doi.org/10.1021/acs.chemrev.2c00410.
[21] M. Haddadnezhad, W. Park, I. Jung, H. Hilal, J. Kim, S. Yoo, Q. Zhao, S. Lee, J. Lee, S. Lee, S. Park, Synthesis of Pt Double-Walled Nanoframes with Well-Defined and Controllable Facets, ACS Nano (2022), https://doi.org/10.1021/acsnano.2c09349.
[22] K.D. Gilroy, X. Yang, S. Xie, M. Zhao, D. Qin, Y. Xia, Shape-Controlled Synthesis of Colloidal Metal Nanocrystals by Replicating the Surface Atomic Structure on the Seed, Adv. Mater. 30 (2018) 1–25, https://doi.org/10.1002/adma.201706312.
[23] L. Zhang, Z. Xie, J. Gong, Shape-controlled synthesis of Au-Pd bimetallic nanocrystals for catalytic applications, Chem. Soc. Rev. 45 (2016) 3916–3934, https://doi.org/10.1039/c5cs00958h.
[24] R.M. Nielsen, S. Murphy, C. Strebel, M. Johansson, I. Chorkendorff, J.H. Nielsen, The morphology of mass selected ruthenium nanoparticles from a magnetron-sputter gas-aggregation source, J. Nanoparticle Res. 12 (2010) 1249–1262, https://doi.org/10.1007/s11051-009-9830-8.
[25] J. Zhao, E. Baibuz, J. Vernieres, P. Grammatikopoulos, V. Jansson, M. Nagel, S. Steinhauer, M. Sowwan, A. Kuronen, K. Nordlund, F. Djurabekova, Formation Mechanism of Fe Nanocubes by Magnetron Sputtering Inert Gas Condensation, ACS Nano 10 (2016) 4684–4694, https://doi.org/10.1021/acsnano.6b01024.
[26] T. Acsente, R.F. Negrea, L.C. Nistor, E. Matei, C. Grisolia, R. Birjega, G. Dinescu, Tungsten nanoparticles with controlled shape and crystallinity obtained by magnetron sputtering and gas aggregation, Mater. Lett. 200 (2017) 121–124, https://doi.org/10.1016/j.matlet.2017.04.105.
[27] M. Vaidulych, J. Hanuš, J. Kousal, S. Kadlec, A. Marek, I. Khalakhan, A. Shelemin, P. Solař, A. Choukourov, O. Kylián, H. Biederman, Effect of magnetic field on the formation of Cu nanoparticles during magnetron sputtering in the gas aggregation cluster source, Plasma Process. Polym. 16 (2019), https://doi.org/10.1002/ppap.201900133.
[28] J. Vernieres, S. Steinhauer, J. Zhao, A. Chapelle, P. Menini, N. Dufour, R.E. Diaz, K. Nordlund, F. Djurabekova, P. Grammatikopoulos, M. Sowwan, Gas Phase Synthesis of Multifunctional Fe-Based Nanocubes, Adv. Funct. Mater. 27 (2017), https://doi.org/10.1002/adfm.201605328.
[29] J. Vernieres, S. Steinhauer, J. Zhao, P. Grammatikopoulos, R. Ferrando, K. Nordlund, F. Djurabekova, M. Sowwan, Site-Specific Wetting of Iron Nanocubes by Gold Atoms in Gas-Phase Synthesis, Adv. Sci. 6 (2019), https://doi.org/10.1002/advs.201900447.
[30] C.M. Wang, D.R. Baer, J.E. Amonette, M.H. Engelhard, Y. Qiang, J. Antony, Morphology and oxide shell structure of iron nanoparticles grown by sputter-gas-aggregation, Nanotechnology 18 (2007), https://doi.org/10.1088/0957-4484/18/25/255603.
[31] A. Vahl, J. Strobel, W. Reichstein, O. Polonskyi, T. Strunskus, L. Kienle, F. Faupel, Single target sputter deposition of alloy nanoparticles with adjustable composition

via a gas aggregation cluster source, Nanotechnology 28 (2017), https://doi.org/10.1088/1361-6528/aa66ef.
[32] J. Drewes, A. Vahl, N. Carstens, T. Strunskus, O. Polonskyi, F. Faupel, Enhancing composition control of alloy nanoparticles from gas aggregation source by in operando optical emission spectroscopy, Plasma Process. Polym. 18 (2021), https://doi.org/10.1002/ppap.202000208.
[33] J. Drewes, S. Ali-Ogly, T. Strunskus, O. Polonskyi, H. Biederman, F. Faupel, A. Vahl, Impact of argon flow and pressure on the trapping behavior of nanoparticles inside a gas aggregation source, Plasma Process. Polym. 19 (2022), https://doi.org/10.1002/ppap.202100125.
[34] J. Drewes, S. Rehders, T. Strunskus, H. Kersten, F. Faupel, A. Vahl, In Situ Laser Light Scattering for Temporally and Locally Resolved Studies on Nanoparticle Trapping in a Gas Aggregation Source, Part. Part. Syst. Char. (2022) 2200112, https://doi.org/10.1002/ppsc.202200112.
[35] J. Kousal, A. Shelemin, M. Schwartzkopf, O. Polonskyi, J. Hanuš, P. Solař, M. Vaidulych, D. Nikitin, P. Pleskunov, Z. Krtouš, T. Strunskus, F. Faupel, S. V. Roth, H. Biederman, A. Choukourov, Magnetron-sputtered copper nanoparticles: lost in gas aggregation and found by in situ X-ray scattering, Nanoscale 10 (2018) 18275–18281, https://doi.org/10.1039/c8nr06155f.
[36] S. Ali-Ogly, J. Kousal, D. Nikitin, P. Pleskunov, J. Hanuš, A. Choukourov, H. Biederman, Computational fluid dynamics predicts the nanoparticle transport in gas aggregation cluster sources, J. Phys. D Appl. Phys. 55 (2022), https://doi.org/10.1088/1361-6463/ac8c4e.
[37] G. Sanzone, J. Yin, K. Cooke, H. Sun, P. Lievens, Impact of the gas dynamics on the cluster flux in a magnetron cluster-source: Influence of the chamber shape and gas-inlet position, Rev. Sci. Instrum. 92 (2021), https://doi.org/10.1063/5.0028854.
[38] J. Zhao, A. Mayoral, L. Martínez, M.P. Johansson, F. Djurabekova, Y. Huttel, Core-Satellite Gold Nanoparticle Complexes Grown by Inert Gas-Phase Condensation, J. Phys. Chem. C 124 (2020) 24441–24450, https://doi.org/10.1021/acs.jpcc.0c07346.
[39] P. Brault, Multiscale molecular dynamics simulation of plasma processing: Application to plasma sputtering, Front. Phys. 6 (2018) 1–7, https://doi.org/10.3389/fphy.2018.00059.
[40] P. Brault, Multiscale molecular dynamics simulations of fuel cell nanocatalyst plasma sputtering growth and deposition, Energies 13 (2020), https://doi.org/10.3390/en13143584.
[41] T. Košutová, L. Horák, P. Pleskunov, J. Hanuš, D. Nikitin, P. Kúš, M. Cieslar, I. Gordeev, S. Burazer, A. Choukourov, M. Dopita, Thermally-driven morphogenesis of niobium nanoparticles as witnessed by in-situ x-ray scattering, Mater. Chem. Phys. 277 (2022), https://doi.org/10.1016/j.matchemphys.2021.125466.
[42] J. Ilavsky, P.R. Jemian, Irena: Tool suite for modeling and analysis of small-angle scattering, J. Appl. Cryst. 42 (2009) 347–353, https://doi.org/10.1107/S0021889809002222.
[43] Z. Matěj, R. Kužel, L. Nichtová, XRD total pattern fitting applied to study of microstructure of TiO 2 films, Powder Diffr. 25 (2010) 125–131, https://doi.org/10.1154/1.3392371.
[44] J.F. Ziegler, M.D. Ziegler, J.P. Biersack, SRIM - The stopping and range of ions in matter (2010), Nucl. Instruments Methods Phys. Res. Sect. B Beam Interact. with Mater. Atoms. 268 (2010) 1818–1823. doi:10.1016/j.nimb.2010.02.091.
[45] N. Matsunami, Y. Yamamura, Y. Itikawa, N. Itoh, Y. Kazumata, S. Miyagawa, K. Morita, R. Shimizu, H. Tawara, Energy dependence of the ion-induced sputtering yields of monatomic solids, At. Data Nucl. Data Tables 31 (1984) 1–80, https://doi.org/10.1016/0092-640X(84)90016-0.
[46] H. Hofsäss, K. Zhang, A. Mutzke, Simulation of ion beam sputtering with SDTrimSP, TRIDYN and SRIM, Appl. Surf. Sci. 310 (2014) 134–141, https://doi.org/10.1016/j.apsusc.2014.03.152.
[47] N. Mahne, M. Čekada, M. Panjan, Total and Differential Sputtering Yields Explored by SRIM Simulations, Coatings 12 (2022) 1–32, https://doi.org/10.3390/coatings12101541.
[48] A. Farhadizadeh, T. Kozák, The importance of discharge voltage in DC magnetron sputtering for energy of sputtered and backscattered atoms on the substrate: Monte-Carlo simulations, Vacuum 196 (2022), https://doi.org/10.1016/j.vacuum.2021.110716.
[49] V.I. Shulga, Note on the artefacts in SRIM simulation of sputtering, Appl. Surf. Sci. 439 (2018) 456–461, https://doi.org/10.1016/j.apsusc.2018.01.039.
[50] J. Rahm, P. Erhart, WulffPack: A Python package for Wulff constructions, J. Open Source Softw. 5 (2020) 1944, https://doi.org/10.21105/joss.01944.
[51] G. Wulff, Xxv. Zur Frage der Geschwindigkeit des Wachsthums und der Auflösung der Krystallflächen, Zeitschrift Für Krist. - Cryst. Mater. 34 (1901) 449–530, https://doi.org/10.1524/zkri.1901.34.1.449.
[52] R. Tran, Z. Xu, B. Radhakrishnan, D. Winston, W. Sun, K.A. Persson, S.P. Ong, Surface energies of elemental crystals, Sci. Data 3 (2016), 160080, https://doi.org/10.1038/sdata.2016.80.
[53] R. Tran, X.G. Li, J.H. Montoya, D. Winston, K.A. Persson, S.P. Ong, Anisotropic work function of elemental crystals, Surf. Sci. 687 (2019) 48–55, https://doi.org/10.1016/j.susc.2019.05.002.
[54] H. Zheng, X.G. Li, R. Tran, C. Chen, M. Horton, D. Winston, K.A. Persson, S.P. Ong, Grain boundary properties of elemental metals, Acta Mater. 186 (2020) 40–49, https://doi.org/10.1016/j.actamat.2019.12.030.
[55] S. Plimpton, Fast Parallel Algorithms for Short-Range Molecular Dynamics, J. Comput. Phys. 117 (1995) 1–19, https://doi.org/10.1006/jcph.1995.1039.
[56] M.R. Fellinger, H. Park, J.W. Wilkins, Force-matched embedded-atom method potential for niobium, Phys. Rev. B - Condens. Matter Mater. Phys. 81 (2010) 1–15, https://doi.org/10.1103/PhysRevB.81.144119.
[57] J. Houska, P. Machanova, M. Zitek, P. Zeman, Molecular dynamics and experimental study of the growth, structure and properties of Zr–Cu films, J. Alloy. Compd. 828 (2020), 154433, https://doi.org/10.1016/j.jallcom.2020.154433.
[58] D. Faken, H. Jónsson, Systematic analysis of local atomic structure combined with 3D computer graphics, Comput. Mater. Sci 2 (1994) 279–286, https://doi.org/10.1016/0927-0256(94)90109-0.
[59] P. Solař, K. Škorvánková, A. Kuzminova, J. Kousal, O. Kylián, Measurement of velocities of copper nanoparticles exiting a gas aggregation source, Vacuum 202 (2022), https://doi.org/10.1016/j.vacuum.2022.111114.
[60] D. Nafday, S. Sarkar, P. Ayyub, T. Saha-Dasgupta, A Reduction in Particle Size Generally Causes Body-Centered-Cubic Metals to Expand but Face-Centered-Cubic Metals to Contract, ACS Nano 12 (2018) 7246–7252, https://doi.org/10.1021/acsnano.8b03360.
[61] A. Wucher, M. Wahl, The formation of clusters during ion induced sputtering of metals, Nucl. Instruments Methods Phys. Res. Sect. B Beam Interact. with Mater. Atoms. 115 (1996) 581–589, https://doi.org/10.1016/0168-583X(96)00153-X.
[62] V.I. Matveev, S.A. Kochkin, Energies, charges, and sizes of clusters under ion sputtering of a metal, J. Exp. Theor. Phys. 110 (2010) 722–729, https://doi.org/10.1134/S1063776110040199.
[63] S.K. Loh, L. Lian, P.B. Armentrout, Collision-induced dissociation of niobium cluster ions: transition-metal-cluster binding energies, J. Am. Chem. Soc. 111 (1989) 3167–3176, https://doi.org/10.1021/ja00191a010.
[64] H. Haberland, History, Some Basics, and an Outlook, in: Y. Huttel (Ed.), Gas-Phase Synth, Wiley-VCH Verlag GmbH, Weinheim, Nanoparticles, 2017.
[65] J.A. Venables, H. Brune, Capture numbers in the presence of repulsive adsorbate interactions, Phys. Rev. B 66 (2002), 195404, https://doi.org/10.1103/PhysRevB.66.195404.
[66] T.A. Witten, L.M. Sander, Diffusion-Limited Aggregation, a Kinetic Critical Phenomenon, Phys. Rev. Lett. 47 (1981) 1400–1403, https://doi.org/10.1103/PhysRevLett.47.1400.
[67] H. Brune, C. Romainczyk, H. Röder, K. Kern, Mechanism of the transition from fractal to dendritic growth of surface aggregates, Nature 369 (1994) 469–471, https://doi.org/10.1038/369469a0.
[68] J. Westergren, H. Grönbeck, S.-G. Kim, D. Tománek, Noble gas temperature control of metal clusters: A molecular dynamics study, J. Chem. Phys. 107 (1997) 3071–3079, https://doi.org/10.1063/1.474662.
[69] M. Bonitz, C. Henning, D. Block, Complex plasmas: a laboratory for strong correlations, Reports Prog. Phys. 73 (2010), 066501, https://doi.org/10.1088/0034-4885/73/6/066501.
[70] L. Zhong, J. Wang, H. Sheng, Z. Zhang, S.X. Mao, Formation of monatomic metallic glasses through ultrafast liquid quenching, Nature 512 (2014) 177–180, https://doi.org/10.1038/nature13617.
[71] J.J. Han, C.P. Wang, X.J. Liu, Y. Wang, Z.-K. Liu, T.-Y. Zhang, J.Z. Jiang, Abnormal correlation between phase transformation and cooling rate for pure metals, Sci. Rep. 6 (2016) 22391, https://doi.org/10.1038/srep22391.
[72] K. Eftaxias, V. Hadjicontis, Analysis of Self-Diffusion Data in V and Nb, Phys. Status Solidi 156 (1989) 393–401, https://doi.org/10.1002/pssb.2221560202.
[73] S. Gauter, F. Haase, P. Solař, O. Kylián, P. Kúš, A. Choukourov, H. Biederman, H. Kersten, Calorimetric investigations in a gas aggregation source, J. Appl. Phys. 124 (2018), https://doi.org/10.1063/1.5037413.
[74] L. Schimka, R. Gaudoin, J. Klimeš, M. Marsman, G. Kresse, Lattice constants and cohesive energies of alkali, alkaline-earth, and transition metals: Random phase approximation and density functional theory results, Phys. Rev. B 87 (2013), 214102, https://doi.org/10.1103/PhysRevB.87.214102.